

Structural distribution in mixed ternary noble gas and Lennard-Jones clusters



Xia Wu^{a,*}, Cuifang Huang^b, Yan Sun^c, Genhua Wu^a

^a School of Chemistry and Chemical Engineering, Anqing Normal University, Anqing 246011, PR China

^b Patent Examination Cooperation Center of SIPO, Jiangsu 215000, PR China

^c College of Chemical Engineering, Hebei United University, Tangshan 063009, PR China

ARTICLE INFO

Article history:

Received 7 November 2012

In final form 19 December 2012

Available online 9 January 2013

Keywords:

Ternary clusters

Lennard-Jones model

Ar–Kr–Xe clusters

Structural optimization

ABSTRACT

The geometrical structures and energies of mixed 38- and 55-atom Ar–Kr–Xe clusters are investigated. The interaction is described by ternary Lennard-Jones (TLJ) potential. The stable structures are optimized by adaptive immune optimization algorithm. Results show that in $\text{Ar}_{12}\text{Kr}_m\text{Xe}_n$ ($m+n=26$) clusters, there exist amorphous and polytetrahedral configurations, and in $\text{Ar}_{13}\text{Kr}_m\text{Xe}_n$ ($m+n=42$) clusters, structures are categorized into four classes, i.e., 8 Mackay icosahedra, 19 amorphous structures, 4 sixfold pancake structures, and 10 ring-like structures. Furthermore, strain energies in Ar–Kr–Xe clusters are studied to propose the possible ways of reducing strain. To investigate the potential energy surface of Ar–Kr–Xe clusters in TLJ model potential, the bond numbers of the $\text{Ar}_{12}\text{Kr}_{13}\text{Xe}_{13}$ cluster and $\text{A}_{12}\text{B}_{13}\text{C}_{13}$ TLJ model potential are compared, and the case of the former one is studied in the bond number phase diagram of the latter one.

© 2012 Elsevier B.V. All rights reserved.

1. Introduction

The structures and properties of noble gas clusters with weak interactions have become a significant problem in the area of molecular spectroscopy and theoretical chemistry. The electronic and geometric structures of noble gas clusters, e.g., Ar, Kr, and Xe clusters, have been widely studied by experiment and theoretical calculations [1–4]. For instance, mass spectra of Ar, Kr, and Xe clusters, grown neutral and ionized by electron impact, up to cluster size $n=1000$ were presented, and the most pronounced “magic numbers” in the distributions of large cluster ions occur at $n=147$ (148 for Ar), 309, and 561 [1]. Clusters of heterogeneous materials show a much richer behavior than their homogeneous counterparts [5], and the geometric and electronic structure of mixed clusters enables studies of photochemistry [6].

The low-energy configurations of noble gas clusters were determined depending on modeling methods. *Ab initio* and DFT methods were used to obtain the variation of the interaction-induced dipole moment, transversal and longitudinal polarizability and the corresponding invariants mean and anisotropy in the Kr–He heterodiatom, and analysis of the performance of the theoretical methods revealed a clear differentiation between *ab initio* and DFT methods [7]. The interaction hyperpolarizability of He_2 , Ne_2 , and He_3 was

discussed using an *ab initio* wave function, McWeeny's coupled Hartree–Fock perturbation theory and an efficient algorithm [8]. Furthermore, collision-induced hyper-Rayleigh spectra of Ne–Ar [9], He–Ne [10], and He–Ar [11] were computed, and the spectral features were discussed. The application of conventional generalized gradient approximation (GGA) and meta-GGA density functionals to van der Waals interactions is fraught with difficulties, and the PW86 exchange, combined with a dynamical correlation GGA and the Becke–Johnson dispersion model, yielded excellent results in noble gas diatomics [12].

On the other hand, Lennard-Jones (LJ) potential was widely applied for the noble gas systems including homogeneous clusters, binary LJ clusters [13,14], ternary LJ (TLJ) [15], clusters and even quinary $\text{Ar}_{11}\text{Kr}_{11}\text{Xe}_{11}\text{He}_{11}\text{Ne}_{11}$ cluster [16]. It has been concluded that mixed noble gas systems can be quite safely described using simple pairwise potentials such as the LJ potential. For example, the effects of mixing different noble gas atoms on cluster structure and thermodynamics have been studied for the specific size 13 by Frantz on the examples of Ar–Kr mixtures [17] as well as Ne–Ar mixtures [18]. A systematic work of Ar–Xe mixed clusters of 13 and 19 atoms has been carried out by Munro and coworkers [19]. The low-energy structures of mixed Ar–Xe and Kr–Xe Lennard-Jones clusters were investigated using Monte Carlo algorithm, and it was found that alloys of dissimilar elements (Ar–Xe) favor polytetrahedral geometries over octahedra (homogeneous clusters) due to the reduced strain penalty. Conversely, octahedra are even more stable in Kr–Xe alloys than in Kr_{38} or Xe_{38} , and

* Corresponding author. Tel./fax: +86 556 550 0090.

E-mail addresses: xiawu@aqtc.edu.cn, xiawu@mail.nankai.edu.cn (X. Wu).

they show a core-surface phase separation behavior [20]. Besides LJ potential with pair interaction, many-body potentials were developed attempting to improve the structural calculations of noble gas clusters and the solid state [21].

Structural phase diagrams are often constructed for the determination of the equilibrium structure of clusters. For instance, to investigate the role of vibrational entropy, Doye et al. drew the phase diagrams of LJ clusters and Sutton–Chen potential for silver clusters showing how the structure depends on both size and temperature, and results showed that they have a very similar form. In Morse potential, well ‘width’ (range) parameter ρ_0 controls the interatomic interaction, and the zero temperature phase diagram showed the variation of the lowest energy structure with atomic size N and parameter ρ_0 [22]. Furthermore, upon atomic size N -atom binary A_lB_m ($l + m = N$) LJ clusters and the ratio parameter (σ_{BB}/σ_{AA} , σ is the finite distance) of pure elemental B- and A-type LJ cluster sizes, structural phase diagram was studied for the stabilization of different structures, particularly polytetrahedral structures [13]. Moreover, for ternary Lennard-Jones (TLJ) $A_lB_mC_n$ clusters, phase diagram upon σ_{BB}/σ_{AA} and σ_{CC}/σ_{AA} , i.e., corresponding parameters of B and C atoms relative to the size parameter σ_{AA} of A atoms, was investigated to study the effect of potential parameters [15].

In this study, the geometrical structures and energies of mixed Ar–Kr–Xe clusters with 38 and 55 atoms are investigated using TLJ potential. Then, the minimum energy configurations of TLJ $A_{12}B_{13}C_{13}$ model cluster with different finite distance parameters are located to investigate the phase diagram of the bond numbers, and the case of $Ar_{12}Kr_{13}Xe_{13}$ cluster is studied in the phase diagram.

2. Method

2.1. Ternary Lennard-Jones potential

Pairwise LJ potential is applied to describe the interatomic interaction in Ar–Kr–Xe clusters, which has been widely investigated. LJ potential is constructed by a long-range attractive part and a short-range repulsive part, and it is given by

$$E = 4\epsilon_{ij} \sum_{1 \leq i < j \leq N} \left[\left(\frac{\sigma_{ij}}{r_{ij}} \right)^{12} - \left(\frac{\sigma_{ij}}{r_{ij}} \right)^6 \right] \\ = \epsilon_{ij} \sum_{1 \leq i < j \leq N} \left[\left(\frac{1}{x_{ij}} \right)^{12} - 2 \left(\frac{1}{x_{ij}} \right)^6 \right] \quad (1)$$

where N is the number of atoms, and r_{ij} represents the distance between atoms i and j ; ϵ_{ij} is the pair well depth, and σ_{ij} is cluster diameter (size). In Ar–Kr–Xe clusters, with respect to argon ($\sigma_{ArAr} = 1.00$, $\epsilon_{ArAr} = 1.00$), the present datum for σ and ϵ are thus $\sigma_{KrKr} = 1.12403$, $\sigma_{XeXe} = 1.206$, $\sigma_{ArKr} = 1.062$, $\sigma_{KrXe} = 1.16397$, $\sigma_{ArXe} = 1.074$, $\epsilon_{KrKr} = 1.373534$, $\epsilon_{XeXe} = 1.852$, $\epsilon_{ArKr} = 1.1717$, $\epsilon_{KrXe} = 1.59914$, and $\epsilon_{ArXe} = 1.48$ [17,20]. In the ternary $A_lB_mC_n$ LJ model, to simplify the parametric form, $\epsilon_{AA} = \epsilon_{BB} = \epsilon_{CC} = \epsilon_{AB} = \epsilon_{AC} = \epsilon_{BC} = 1.00$ with reduced units are used. With respect to A atoms (σ_{AA} is set as 1.00), σ_{BB} , σ_{CC} , σ_{AB} , σ_{AC} , and σ_{BC} are the variable parameters. Furthermore, σ_{ij} can be determined by a set of combining rules, and it is quite common to use an arithmetic mean (Lorentz rule): $\sigma_{ij} = (\sigma_{ii} + \sigma_{jj})/2$. Thus, σ_{AB} , σ_{AC} , and σ_{BC} are determinate if σ_{AA} , σ_{BB} , and σ_{CC} are given, and only two parameters σ_{BB} and σ_{CC} are variable [15].

2.2. Optimization method

The minimum energy structures of TLJ clusters are located by using AIOA, which is an adaptive heuristic search algorithm based on the evolutionary ideas of natural genetic selection and clonal

selection principles similar to genetic algorithm (GA) [23–25]. AIOA has been successfully proposed for the optimization of mono-elemental clusters, e.g., LJ_{200} clusters [26,27]. The modified AIOA was developed for binary clusters, such as Cu–Au and Ag–Au clusters [28], and ternary clusters, e.g., Cu–Ag–Au trimetallic clusters [29] and TLJ clusters [15]. The basic steps of the AIOA include the construction of original gene library, immune clone operation, and mutation operation. In the immune clone selection procedure, a population of individuals is selected, and the selected individuals are performed by the mutation operation to select new individuals. With respect to the modified AIOA for binary and ternary clusters, in the mutation operation, 50% of the individuals are selected with energy-based mutation to geometrical isomers, and the other 50% individuals are performed with atom exchange operation, i.e., two type atoms are selected randomly and their location is exchanged solving ‘‘homotopic’’ isomers problem [24]. With the repetition of the selection, mutation, and updating gene library operations, the stable structure of a ternary cluster is optimized by the modified AIOA.

3. Results and discussion

3.1. Composition-induced transitions in $Ar_{12}Kr_mXe_n$ ($m + n = 26$) clusters

Putative stable structures of $Ar_{12}Kr_mXe_n$ ($m + n = 26$) clusters are obtained, and the optimized structures are plotted in Fig. 1. From the figure, two types, i.e., amorphous and polytetrahedron [30], of the minimum energy configurations can be found. With the size m from 1 to 4, the configuration of clusters is amorphous. It is clear that Kr atoms are distributed on the surface of the structure, and Ar and Xe atoms are irregularly mixed on the surface and in the inner. However, for m from 5 to 25, it can be seen that all

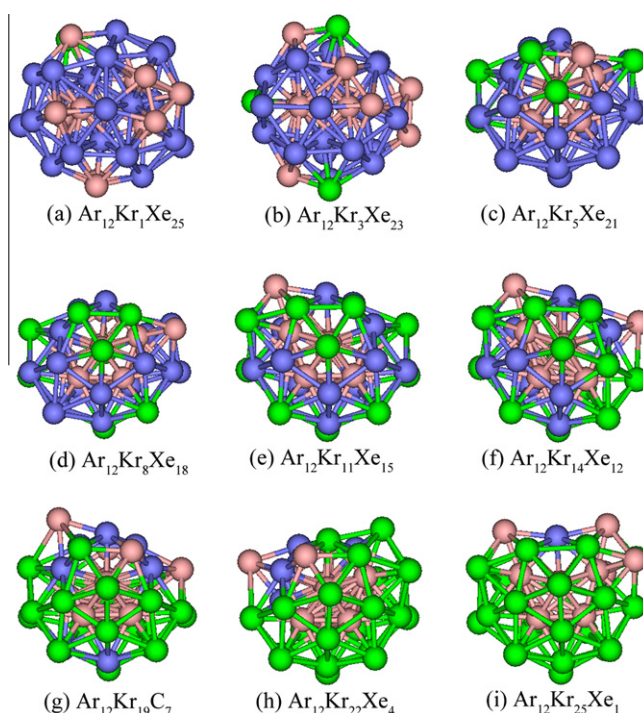


Fig. 1. Typical putative stable structures of $Ar_{12}Kr_mXe_n$ ($m + n = 26$) clusters, and Ar, Kr, and Xe atoms are represented by pink, green, and blue spheres, respectively. (For interpretation of the references to color in this figure legend, the reader is referred to the web version of this article.)

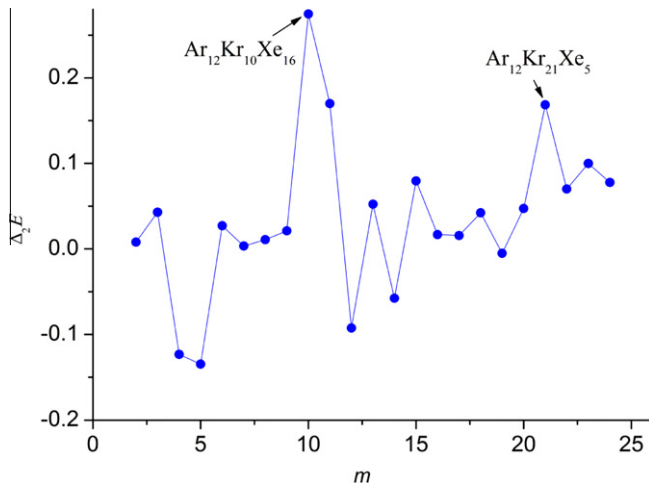


Fig. 2. Second finite differences of the energies of the optimized $\text{Ar}_{12}\text{Kr}_m\text{Xe}_n$ ($m + n = 26$) clusters.

clusters have polytetrahedral structures from the figure. By a comparison of the structures, the inner core of the polytetrahedral configuration is found to be an icosahedron, and it is almost composed with most Ar atoms with one or two Ar atoms on the surface. On the other hand, with the increasing size of m , Kr and Xe atoms are distributed on the surface of the structures as in $m = 1-4$.

Previous study by Calvo and Yurtsever [20] has shown that in 38-atom Ar–Xe and Kr–Xe clusters, homogeneous Ar, Kr, and Xe clusters had a truncated octahedral shape, and Ar–Xe clusters favored polytetrahedral geometries over octahedral. However, in 38-atom Kr–Xe clusters, octahedra were even more stable than in Kr_{38} and Xe_{38} , showing a core (Kr)–surface (Xe) separation behavior. The significant trend of core/surface phase separation was also found in Ar–Xe clusters for the number of Xe atoms larger than 20, and conversely, for number of Xe atoms smaller than 20, clusters exhibit a degree of mixing. However, because of ternary elemental mixed clusters, in the $\text{Ar}_{12}\text{Kr}_m\text{Xe}_n$ ($m + n = 26$) clusters, when $m > 5$, there exhibits core (Ar)–surface (Kr and Xe) separation. The separation of Kr and Xe atoms as in 38-atom Kr–Xe clusters is insignificant, and it may be found in larger size clusters.

On the other hand, to analyze the stability of a cluster of a certain composition comparing to its neighbors, the second finite difference of the energy is applied as a quantitative function. Fig. 2 plots the second difference, $\Delta_2 E = E_{N+1} + E_{N-1} - 2E_N$, as a function of a 38-atom $\text{A}_{12}\text{B}_m\text{C}_n$ ($m + n = 26$) clusters with size m . In the figure, the positive peaks indicate particularly stable structures with respect to their neighbors, and from the results of the second difference two apparent positive peaks, i.e., $\text{Ar}_{12}\text{Kr}_{10}\text{Xe}_{16}$ and $\text{Ar}_{12}\text{Kr}_{21}\text{Xe}_5$, are found in the curve, which may be relatively more stable. Due to the low point group (PG) symmetry, the stability is hard to be explained considering rare reports.

3.2. Stable structures of $\text{Ar}_{13}\text{Kr}_m\text{Xe}_n$ ($m + n = 42$) clusters

The putative stable structures of 55-atom $\text{Ar}_{13}\text{Kr}_m\text{Xe}_n$ ($m + n = 42$) clusters are investigated, and several typical structures are shown in Fig. 3. These 41 structures can be categorized into four classes, i.e., 8 Mackay icosahedra (Ih) for $m = 1-6$ and 40–41, 19 amorphous structures for $m = 7-25$, 4 sixfold pancake structures at $m = 26-29$, and 10 ring-like structures linked by three face-sharing double icosahedra [15] for $m = 30-39$.

For the clusters of $\text{Ar}_{13}\text{Kr}_m\text{Xe}_n$ ($m = 1-6$), the central atom of icosahedra is Ar. At $\text{Ar}_{13}\text{Kr}_1\text{Xe}_{41}$ and $\text{Ar}_{13}\text{Kr}_2\text{Xe}_{40}$, the extra 12 Ar atoms occupy all 12 vertex sites of the icosahedra, and one and

two Kr atoms are located in the inner-shell. However, at $\text{Ar}_{13}\text{Kr}_3\text{Xe}_{39}$, three Kr atoms occupy the surface sites, with two Kr atoms on the vertex sites and the third Kr atom on the surface making the (111) face of the icosahedron distorted. For the structure of $\text{Ar}_{13}\text{Kr}_4\text{Xe}_{38}$, three Kr atoms are located in the inner-shell. At $\text{Ar}_{13}\text{Kr}_5\text{Xe}_{37}$ and $\text{Ar}_{13}\text{Kr}_6\text{Xe}_{36}$, four and five Kr atoms occupy the vertex sites, and one Kr atom is located on the surface and in the inner-shell, respectively. For the clusters of $\text{Ar}_{13}\text{Kr}_m\text{Xe}_n$ ($m = 7-25$), most Ar atoms are in the inner-shell, and Kr and Xe atoms are irregularly segregated on the surface, except for one Kr atom in the inner-shell for $\text{Ar}_{13}\text{Kr}_{23}\text{Xe}_{19}$. Furthermore, in $\text{Ar}_{13}\text{Kr}_m\text{Xe}_n$ ($m = 26-29$) clusters, there exist almost the same sixfold pancake frame taken from $\text{Ar}_{13}\text{Kr}_{27}\text{Xe}_{15}$ as shown in Fig. 4, and the sixfold motif was also found in Morse potential [31], modified Morse potential [32], and two-center Lennard-Jones clusters [33]. In the frame, the central atom is Kr, and it is surrounded by Ar atoms. The 12-atom Ar frame is further surrounded by Kr atoms, and its top and bottom sites are occupied by 7 Xe atoms, respectively. At $\text{Ar}_{13}\text{Kr}_{26}\text{Xe}_{16}$, one extra Xe atom occupies the site occupied by Kr atom at $\text{Ar}_{13}\text{Kr}_{27}\text{Xe}_{15}$. Comparing with $\text{Ar}_{13}\text{Kr}_{27}\text{Xe}_{15}$, the absent sites of Xe atoms at $\text{Ar}_{13}\text{Kr}_{28}\text{Xe}_{14}$ and $\text{Ar}_{13}\text{Kr}_{29}\text{Xe}_{13}$ are occupied by Kr atoms. Therefore, in $\text{Ar}_{13}\text{Kr}_m\text{Xe}_n$ ($m = 26-29$) clusters, Kr and Xe atoms are significantly segregated.

With the increase of m values from 30 to 39, clusters have ring-like structures linked by three face-sharing double icosahedra. The central atom is Xe, and most of Ar atoms are in the inner. Kr and other Xe atoms prefer on the surface tending to a segregation form. However, at $\text{Ar}_{13}\text{Kr}_{40}\text{Xe}_2$ and $\text{Ar}_{13}\text{Kr}_{41}\text{Xe}_1$, the motif of clusters is Mackay icosahedron with two and one Xe atoms on the surface, and the distribution of Ar atoms is similar with those in $\text{Ar}_{13}\text{Kr}_m\text{Xe}_n$ ($m = 1-2$) clusters. It can be concluded that Ar atoms prefer in the inner core for $m = 7-39$, however in icosahedral structures, Ar atoms tend to occupy the vertex sites. Moreover, the segregation phenomenon of Kr and Xe atoms occurs with the increase of m from 7 to 41.

Fig 5 plots the second finite difference of the energy as a function of $\text{A}_{13}\text{B}_m\text{C}_n$ ($m + n = 42$) clusters with size m . From the figure, eight apparent positive peaks, i.e., $m = 4, 7, 9, 22, 24, 29, 31$, and 36, are found in the curve, and they may have relatively more stable structures.

3.3. Reduced strain energies in Ar–Kr–Xe clusters

The role of heterogeneity on the strain is calculated for the various contributions to the reduced strain energies in Ar–Kr–Xe clusters. The strain energies are defined for Ar–Ar, Kr–Kr, Xe–Xe, Ar–Kr, Ar–Xe, and Kr–Xe interactions as follows [34]:

$$E_{\text{Ar–Ar}}^{\text{strain}} = E_{\text{Ar–Ar}} + n_{\text{Ar–Ar}}^{\text{nn}} \epsilon_{\text{Ar–Ar}} \quad (2)$$

$$E_{\text{Kr–Kr}}^{\text{strain}} = E_{\text{Kr–Kr}} + n_{\text{Kr–Kr}}^{\text{nn}} \epsilon_{\text{Kr–Kr}} \quad (3)$$

$$E_{\text{Xe–Xe}}^{\text{strain}} = E_{\text{Xe–Xe}} + n_{\text{Xe–Xe}}^{\text{nn}} \epsilon_{\text{Xe–Xe}} \quad (4)$$

$$E_{\text{Ar–Kr}}^{\text{strain}} = E_{\text{Ar–Kr}} + n_{\text{Ar–Kr}}^{\text{nn}} \epsilon_{\text{Ar–Kr}} \quad (5)$$

$$E_{\text{Ar–Xe}}^{\text{strain}} = E_{\text{Ar–Xe}} + n_{\text{Ar–Xe}}^{\text{nn}} \epsilon_{\text{Ar–Xe}} \quad (6)$$

$$E_{\text{Kr–Xe}}^{\text{strain}} = E_{\text{Kr–Xe}} + n_{\text{Kr–Xe}}^{\text{nn}} \epsilon_{\text{Kr–Xe}} \quad (7)$$

In these equations, $E_{\text{X–Y}}$ is the total binding energy between atoms X and Y, and $\epsilon_{\text{X–Y}}$ is the Lennard-Jones well depth corresponding to the interaction between X and Y atoms. The number of the nearest neighbor contacts (n^{nn}), that is the number of bonds, is an important property of clusters, and the number for the clusters is generally used to distinguish the degree of packing. n^{nn} is given by

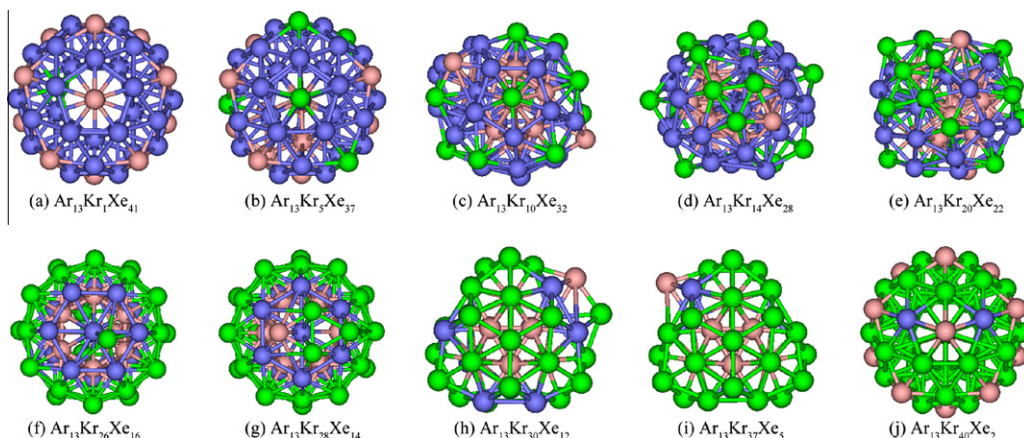


Fig. 3. Typical putative stable structures of $\text{Ar}_{13}\text{Kr}_m\text{Xe}_n$ ($m+n=42$) clusters, and Ar, Kr, and Xe atoms are represented by pink, green, and blue spheres, respectively. (For interpretation of the references to color in this figure legend, the reader is referred to the web version of this article.)

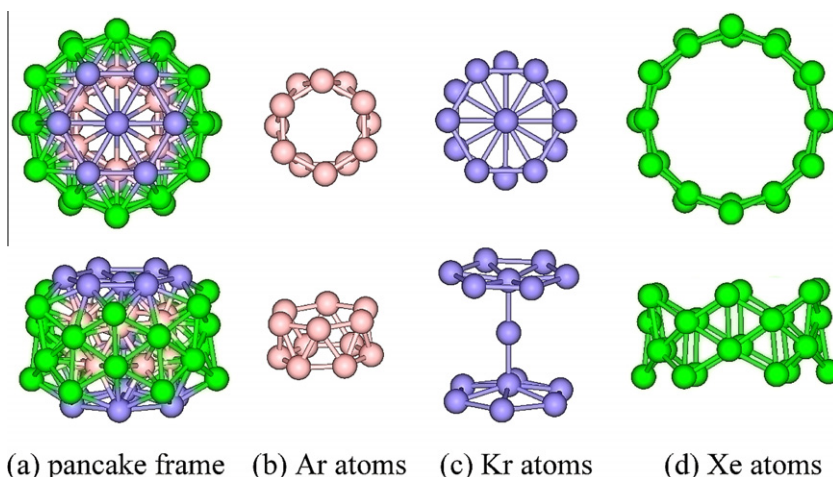


Fig. 4. Inner pancake frame in $\text{Ar}_{13}\text{Kr}_m\text{Xe}_n$ ($m=26-28$) clusters, and Ar, Kr, and Xe atoms are represented by pink, green, and blue spheres, respectively. (For interpretation of the references to color in this figure legend, the reader is referred to the web version of this article.)

$$n^{nn} = \sum_{i < j} \delta_{ij} \quad (8)$$

where $\delta_{ij} = \begin{cases} 1, & r_{ij} \leq 1.2r_m \\ 0, & r_{ij} > 1.2r_m \end{cases}$ $i, j = \text{A, B, or C}$, and r_m is a nearest neighbor criterion.

Reduced strain energies are then defined as $e^{\text{strain}} = E^{\text{strain}}/n^{nn}e$, in order to account for the different magnitudes of the interactions among atom types. The strain energies in $\text{Ar}_{12}\text{Kr}_m\text{Xe}_n$ ($m+n=26$) clusters and $\text{Ar}_{13}\text{Kr}_m\text{Xe}_n$ ($m+n=42$) clusters are represented with size m in Fig. 6, and it can be seen that they are always positive values according to these definitions. They may give us some insight about the possible ways of reducing strain.

From Fig. 6a, it is clear that for $m=1-4$, the total strain energies of all bonds are lowest, and their structures have been determined as amorphous. However, for $m=5-25$, polytetrahedral structures have relatively high strain energies. It can be accounted for by high Ar–Ar strain energies in the figure. In $\text{Ar}_{13}\text{Kr}_m\text{Xe}_n$ ($m+n=42$) clusters of Fig. 6b, for $m=1, 2, 5, 6, 40$, and 41, i.e., icosahedral structures, $m=23$ and 24, i.e., several amorphous structures, $m=26-29$, i.e., 4 sixfold pancake structures, the strain energies are relatively low. However, in the area of high strain energies, e.g., $m=12-22$, the Ar–Ar and Ar–Kr bonds generate a high strain energy. Furthermore, in ring-like structures, i.e., $m=32-39$, Ar–Ar and Xe–Xe bonds affect the strain energies. Therefore, Ar–Ar and Xe–Xe bonds may play an important effect on the strain energy.

3.4. Analysis of $\text{Ar}_{12}\text{B}_{13}\text{C}_{13}$ TLJ model with different σ_{BB}/σ_{AA} and σ_{CC}/σ_{AA}

The cluster of $\text{Ar}_{12}\text{Kr}_{13}\text{Xe}_{13}$ is taken as an example to investigate the potential energy surface of Ar–Kr–Xe clusters in TLJ model po-

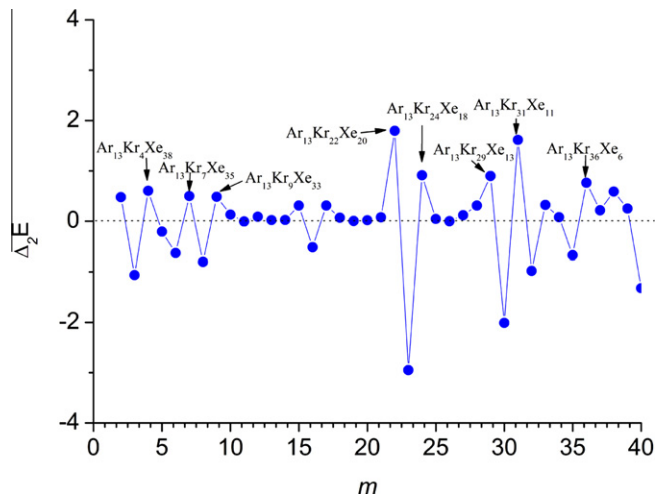


Fig. 5. Second finite differences of the energies of the optimized $\text{Ar}_{13}\text{Kr}_m\text{Xe}_n$ ($m+n=42$) clusters.

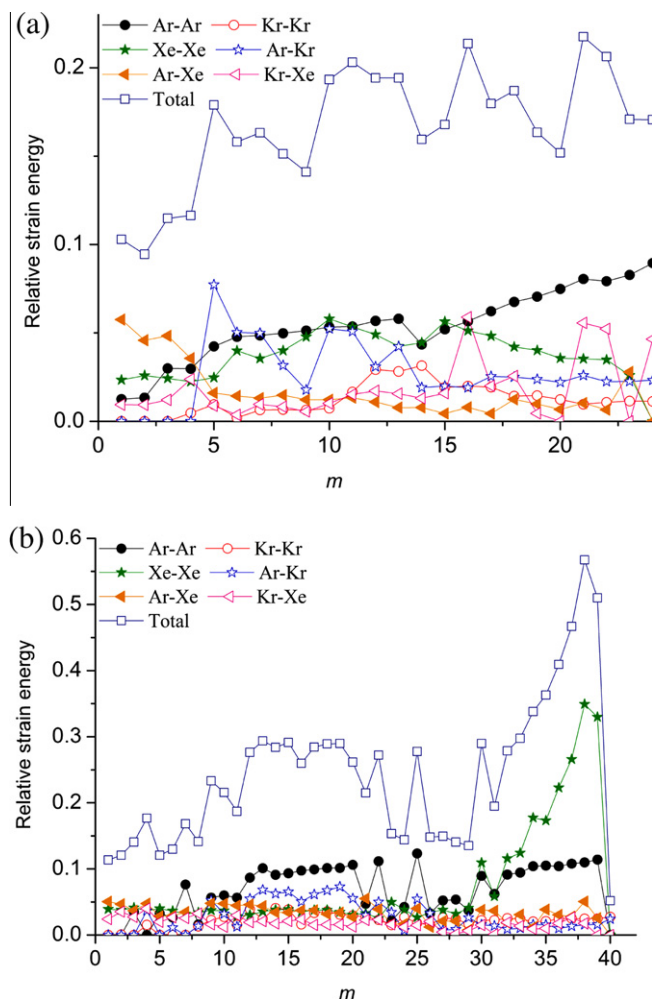


Fig. 6. Reduced strain energies for Ar–Ar, Kr–Kr, Xe–Xe, Ar–Kr, Ar–Xe, and Kr–Xe interactions in (a) $\text{Ar}_{12}\text{Kr}_m\text{Xe}_n$ ($m+n=26$) clusters and (b) $\text{Ar}_{13}\text{Kr}_m\text{Xe}_n$ ($m+n=42$) clusters.

tential [35], and the bond numbers of the $\text{Ar}_{12}\text{Kr}_{13}\text{Xe}_{13}$ cluster and $\text{A}_{12}\text{B}_{13}\text{C}_{13}$ model potential are compared. The putative stable structures of $\text{A}_{12}\text{B}_{13}\text{C}_{13}$ clusters with $\sigma_{\text{BB}}/\sigma_{\text{AA}}$ and $\sigma_{\text{CC}}/\sigma_{\text{AA}}$ both from 1.00 to 1.40 are investigated by AIOA, and some typical optimized structures are shown in Fig. 7. From the figure, four types of the minimum energy configurations can be found, i.e., truncated octahedron (Fig. 7a), partial Mackay icosahedron (Fig. 7b), polytetrahedron (Fig. 7c and d), and fivefold pancake structure (Fig. 7e). At first, the truncated octahedral structure is only found at

$\sigma_{\text{BB}}/\sigma_{\text{AA}} = 1.00$ and $\sigma_{\text{CC}}/\sigma_{\text{AA}} = 1.02$, and partial Mackay icosahedral structure is only found at $\sigma_{\text{BB}}/\sigma_{\text{AA}} = 1.00$ and $\sigma_{\text{CC}}/\sigma_{\text{AA}} = 1.04$. Furthermore, most of clusters have polytetrahedral structures, and the dominant motif is shown in Fig. 7d. From Fig. 7d, it can be seen that 12 A atoms in the structure almost compose an icosahedron. However, in the fivefold pancake structure of Fig. 7e, A atoms almost compose a Marks' decahedron [36]. Moreover, even for the clusters with the same polytetrahedral configuration, there exists a homotopic change (the location of B and C atoms) with the variable $\sigma_{\text{BB}}/\sigma_{\text{AA}}$ and $\sigma_{\text{CC}}/\sigma_{\text{AA}}$ values. Clearly, the potential range can affect the global minimum structures. As discussed in Ref. [32], for 38-atom modified Morse potential, the structural phase diagram shows the variation of the lowest energy structure with parameter ρ and ϕ controlling the long- and short-range interactions. Depending on ρ and ϕ , face-centered cubic (fcc) structure was found at the short-range, e.g., truncated octahedron, as in this study. Furthermore, with the increasing of the potential range at the long range or the decreasing of the potential range at the short range, there exist 13-atom Ih-based poly-Ih structure, and sixfold poly-Ih structure, and the similar structural distribution is also found in this study, such as partial Ih, polytetrahedron, and fivefold pancake structure.

Fig. 8 shows the numbers (n^{mm}) of A–A, A–B, B–B, and B–C bonds in $\text{A}_{12}\text{B}_{13}\text{C}_{13}$ clusters with the variation of $\sigma_{\text{BB}}/\sigma_{\text{AA}} = 1.00$ –1.40 and $\sigma_{\text{CC}}/\sigma_{\text{AA}} = 1.00$ –1.40, which is calculated according to Eq. (8) [37,38]. Because of the same number of B and C atoms, the numbers of A–A, A–B, B–B, and B–C bonds are adopted to analyze the atomic distribution of A, B, and C atoms in the TLJ clusters with different σ values. At first, from the numbers of A–A bonds, it can be seen that along the vertical direction of $\sigma_{\text{BB}}/\sigma_{\text{AA}} = \sigma_{\text{CC}}/\sigma_{\text{AA}}$, the numbers are symmetrically arranged. It is the reason that B and C atoms have the same proportion of 1:1 and the same variable σ values. Furthermore, it is clear that most of clusters have polytetrahedral structures with 36 A–A bonds as discussed in Fig. 7d. Number 31 in the figure indicates that clusters have the fivefold structures as in Fig. 7e. Moreover, Numbers 26, 30, and 34 show that the structures change from partial Mackay icosahedron (Fig. 7b) to polytetrahedral structure with A atoms amorphous (Fig. 7c) to polytetrahedral structure with A atoms partial icosahedron (Fig. 7d). The structural variation can also be found from the numbers of A–B bonds. From the number of A–B bonds, the dominant numbers are 42 and 21, and it shows that in the area of $2.42 < \sigma_{\text{CC}}/\sigma_{\text{AA}} + \sigma_{\text{BB}}/\sigma_{\text{AA}} < 2.64$, their A and B atoms have the same atomic distribution in the clusters. When $\sigma_{\text{CC}}/\sigma_{\text{AA}} + \sigma_{\text{BB}}/\sigma_{\text{AA}} < 2.42$, the variation of atomic distribution is significant. On the other hand, it can be deduced that with the increase of σ values, the numbers of A–C bonds should change contrary to those of A–B bonds along with the vertical direction of $\sigma_{\text{BB}}/\sigma_{\text{AA}} = \sigma_{\text{CC}}/\sigma_{\text{AA}}$. Next, the number of B–B is contrary to that of C–C bonds, and the average number of B–B and C–C bonds is significantly smaller than that

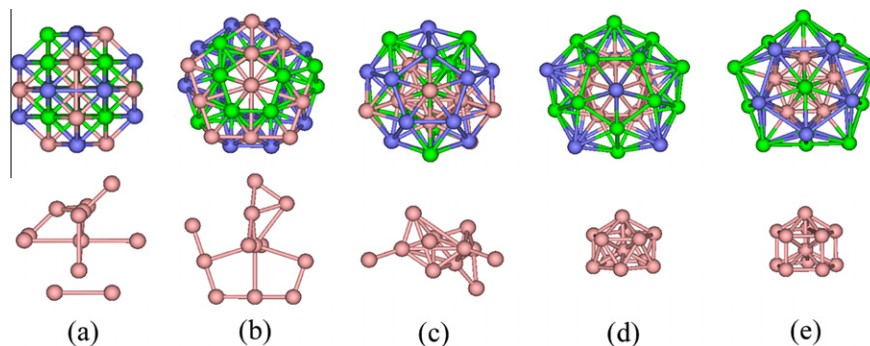


Fig. 7. Typical structures in $\text{A}_{12}\text{B}_{13}\text{C}_{13}$ clusters with $\sigma_{\text{BB}}/\sigma_{\text{AA}}$ and $\sigma_{\text{CC}}/\sigma_{\text{AA}}$ both from 1.00 to 1.40.

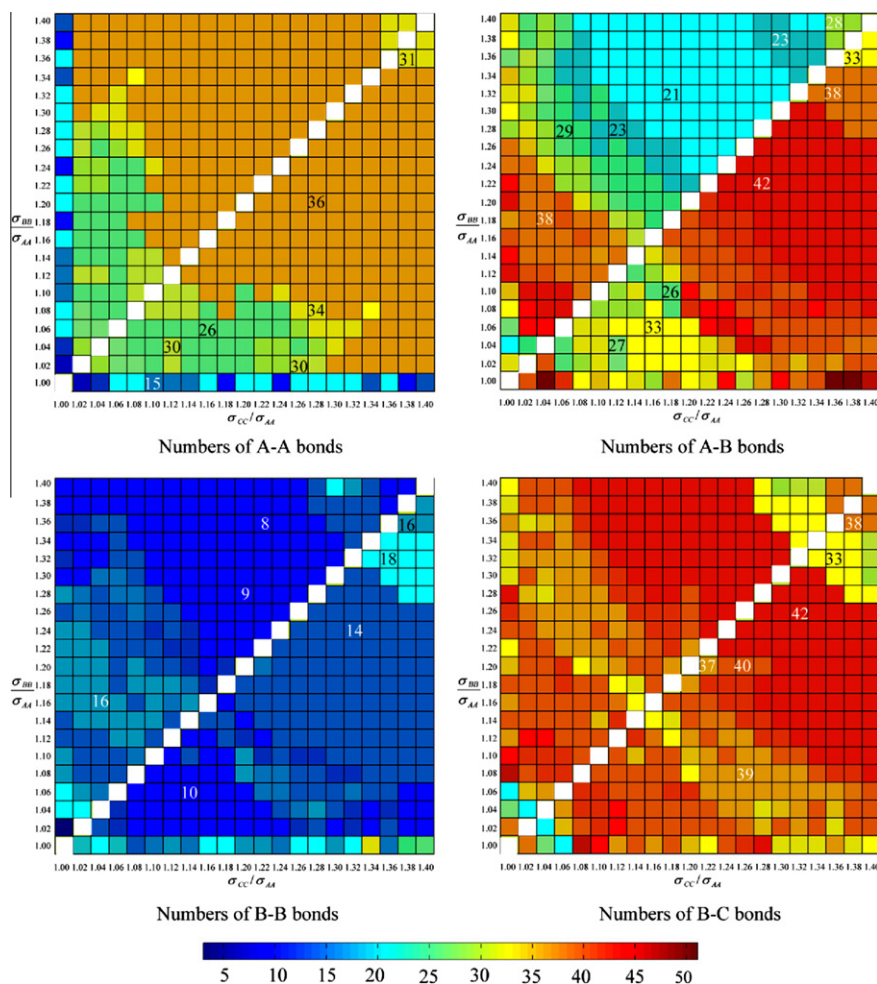


Fig. 8. Number of A-A, B-B, A-B, and B-C bonds in TLJ $A_{12}B_{13}C_{13}$ clusters with σ_{BB}/σ_{AA} and σ_{CC}/σ_{AA} values ranging from 1.00 to 1.40. The labeled numbers stand for the numbers of bonds.

of A-A bonds. It is demonstrated that B and C atoms tend to be on the surface of clusters. Furthermore, from the large number of B-C bonds, it can be concluded that B and C atoms are well mixed as discussed above. With the increase of σ_{BB}/σ_{AA} and σ_{CC}/σ_{AA} , most of the numbers is larger than 35.

On the other hand, the number of Ar-Ar, Kr-Kr, Xe-Xe, Ar-Kr, Ar-Xe, and Kr-Xe bonds is 30, 13, 15, 19, 47, and 37 in $Ar_{12}Kr_{13}Xe_{13}$ cluster, respectively. By the comparison of $Ar_{12}Kr_{13}Xe_{13}$ cluster and $A_{12}B_{13}C_{13}$ model potential, the former one can be found in the area $\sigma_{BB}/\sigma_{AA} + \sigma_{CC}/\sigma_{AA} = 2.16$ – 2.26 of the latter one.

4. Conclusion

The stable structures of $Ar_{12}Kr_mXe_n$ ($m+n=26$) clusters and $Ar_{13}Kr_mXe_n$ ($m+n=42$) clusters has been optimized by ternary Lennard-Jones (TLJ) potential, and results showed that in $Ar_{12}Kr_mXe_n$ ($m+n=26$) clusters, there existed amorphous and polytetrahedron two minimum energy configurations, and in $Ar_{13}Kr_mXe_n$ ($m+n=42$) clusters, structures could be categorized into four classes, i.e., 8 Mackay icosahedra, 19 amorphous structures, 4 sixfold pancake structures, and 10 ring-like structures linked by three face-sharing double icosahedra. Furthermore, the reduced strain energies in Ar-Kr-Xe clusters were studied, and it was found that Ar-Ar and Xe-Xe bonds might play an important effect on the strain energy to propose the possible ways of reducing strain. Moreover, the bond numbers of the $Ar_{12}Kr_{13}Xe_{13}$ cluster and the

bond number phase diagram of $A_{12}B_{13}C_{13}$ model potential are compared, and the case of $Ar_{12}Kr_{13}Xe_{13}$ cluster was studied in this phase diagram.

Acknowledgments

This study is supported by National Natural Science Foundation of China (NNSFC) (Grant Nos. 21203002 and 21171008). The authors thank X.G. Shao for a grant of AIOA program from Nankai University.

References

- [1] W. Miehe, O. Kandler, T. Leisner, O. Echt, J. Chem. Phys. 91 (1989) 5940.
- [2] B.W. van de Waal, J. Chem. Phys. 98 (1993) 4909.
- [3] S.K. Gregurick, M.H. Alexander, B. Hartke, J. Chem. Phys. 104 (1996) 2684.
- [4] D. Bressanini, G. Morosi, J. Phys. Chem. A 115 (2011) 10880.
- [5] R. von Pietrowski, K. von Haefen, T. Laarmann, T. Moller, L. Museur, A.V. Kanaev, Eur. Phys. J. D 38 (2006) 323.
- [6] A. Lindblad, T. Rander, I. Bradeanu, G. Öhrwall, O. Björneholm, M. Mucke, V. Ulrich, T. Lischke, U. Hergenrohn, Phys. Rev. B 83 (2011) 125414.
- [7] D. Xenides, A. Hantzis, G. Maroulis, Chem. Phys. 382 (2011) 80.
- [8] M.G. Papadopoulos, J. Waite, Chem. Phys. Lett. 135 (1987) 361.
- [9] W. Glaz, T. Bancewicz, J. Chem. Phys. 118 (2003) 6264.
- [10] W. Glaz, T. Bancewicz, J.L. Godet, G. Maroulis, A. Haskopoulos, Phys. Rev. A 73 (2006) 042708.
- [11] G. Maroulis, A. Haskopoulos, W. Glaz, T. Bancewicz, J.L. Godet, Chem. Phys. Lett. 428 (2006) 28.
- [12] F.O. Kannemann, A.D. Becke, J. Chem. Theory Comput. 6 (2010) 1081.
- [13] J.P.K. Doye, L. Meyer, Phys. Rev. Lett. 95 (2005) 063401.
- [14] V.K. de Souza, D.J. Wales, J. Chem. Phys. 130 (2009) 194508.

- [15] X. Wu, Y. Sun, C.S. Li, W. Yang, J. Phys. Chem. A 116 (2012) 8218.
- [16] J.M. Dieterich, B. Hartke, J. Comput. Chem. 32 (2011) 1377.
- [17] D.D. Frantz, J. Chem. Phys. 105 (1996) 10030.
- [18] D.D. Frantz, J. Chem. Phys. 107 (1997) 1992.
- [19] L.J. Munro, A. Tharrington, K.J. Jordan, Comp. Phys. Comm. 145 (2002) 1.
- [20] F. Calvo, E. Yurtsever, Phys. Rev. B 70 (2004) 045423.
- [21] P. Schwerdtfeger, N. Gaston, R.P. Krawczyk, R. Tonner, G.E. Moyano, Phys. Rev. B 73 (2006) 064112.
- [22] J.P.K. Doye, D.J. Wales, J. Chem. Soc. Faraday Trans. 93 (1997) 4233.
- [23] D.M. Deaven, N. Tit, J.R. Morris, K.M. Ho, Chem. Phys. Lett. 256 (1996) 195.
- [24] L.D. Lloyd, R.L. Johnston, C. Roberts, T.V. Mortimer-Jones, Chem. Phys. Chem. 3 (2002) 408.
- [25] R. Ferrando, J. Jellinek, R.L. Johnston, Chem. Rev. 108 (2008) 845.
- [26] X.G. Shao, L.J. Cheng, W.S. Cai, J. Chem. Phys. 120 (2004) 11401.
- [27] L.J. Cheng, W.S. Cai, X.G. Shao, Chem. Phys. Lett. 389 (2004) 309.
- [28] X. Wu, W.S. Cai, X.G. Shao, J. Comput. Chem. 30 (2009) 1992.
- [29] X. Wu, G.H. Wu, Y.C. Chen, Y.Y. Qiao, J. Phys. Chem. A 115 (2011) 13316.
- [30] D.R. Nelson, F. Spaepen, Solid State Phys. 42 (1989) 1.
- [31] L.J. Cheng, J.L. Yang, J. Phys. Chem. A 111 (2007) 5287.
- [32] L.J. Cheng, J.L. Yang, J. Chem. Phys. 127 (2007) 124104.
- [33] Y. Feng, J. Wu, L.J. Cheng, H.Y. Liu, J. Chem. Phys. 135 (2011) 244108.
- [34] J.P.K. Doye, D.J. Wales, R.S. Berry, J. Chem. Phys. 103 (1995) 4234.
- [35] L.J. Cheng, W.S. Cai, X.G. Shao, Chem. Phys. Chem. 8 (2007) 569.
- [36] L.D. Marks, Phil. Mag. A 49 (1984) 81.
- [37] J.P.K. Doye, F. Calvo, Phys. Rev. Lett. 86 (2001) 3570.
- [38] P.A. Frantsuzov, V.A. Mandelshtam, Phys. Rev. E 72 (2005) 037102.